Peeling of finite-length elastica on Winkler foundation until complete detachment

Raymond H. Plaut [a,*], Dohgyu Hwang [b,c], Chanhong Lee [b], Michael D. Bartlett [b,c], David A. Dillard [c,d]

[a] *Department of Civil and Environmental Engineering, Virginia Tech, Blacksburg, VA 24061, USA*
[b] *Department of Mechanical Engineering, Soft Materials and Structures Lab, Virginia Tech, Blacksburg, VA 24061, USA*
[c] *Macromolecules Innovation Institute, Virginia Tech, Blacksburg, VA 24061, USA*
[d] *Department of Biomedical Engineering and Mechanics, Virginia Tech, Blacksburg, VA 24061, USA*

ARTICLE INFO

ABSTRACT

Quasi-static peeling of a finite-length, flexible, horizontal beam (strip, thin film) from a horizontal substrate is considered. The displaced end of the beam is subjected to an upward deflection or to a rotation. The action of the adhesive is modeled as a Winkler foundation, and debonding is based on the common fracture mechanics approach. The behavior is examined from the application of loading to the initiation of peeling and then to complete detachment of the beam from the substrate. During at least a portion of the debonding process, the model corresponds to what traditionally has been considered a short beam on an elastic foundation. In the analysis, the beam is modeled as an elastica, so that bending is paramount and large displacements are allowed. The effects of the relative foundation stiffness to the beam bending stiffness, the work of adhesion, and the length, self-weight, extensibility, and initial unbonded length of the beam are investigated. In addition, experiments are conducted to complement the analysis.

1. Introduction

Some recent papers on peeling have been motivated by the gecko and other wall-climbing animals (e.g., Pesika et al., 2007; Sekiguchi et al., 2012; 2014; Williams, 2015; Tysoe and Spencer, 2015; Wu et al., 2015; Gu et al., 2016; Skopic and Schniepp, 2020; Gouravaraju et al., 2021; Wang et al., 2021). The problem of detachment is sometimes modeled as peeling of a beam until it completely separates from the substrate, which is the topic of the present study.

A paper by Peng et al. (2019) discusses peeling and complete detachment of finite-length beams lifted by a vertical force F at one end. The substrate is not modeled as an elastic foundation. Rather, a traction-separation law is used for beam deflections from the rigid substrate, using (i) an exponential form in an elastica analysis or (ii) a bilinear cohesive zone in a finite element analysis. Equilibrium paths are presented (corresponding to F versus δ in the notation in Fig. 1(b)). The effects of the initial unbonded length (a_0 in Fig. 1(a)), a beam stiffness parameter, and a beam thinness parameter are investigated.

Other similar studies to the present one include papers that model a

carbon nanotube as an elastica and examine complete detachment from a rigid substrate. Two papers involve a vertical force applied to a free end of the elastica. One is Buchoux et al. (2011), in which a JKR-type of debonding criterion is utilized, which specifies the curvature at the peel front in terms of the work of adhesion and the bending stiffness of the elastica. The elastica is almost straight and vertical when complete detachment is imminent. The other paper is Fu and Zhang (2011), where the interactive force between the elastica and the substrate is modeled as a van der Waals force. A sequence of four shapes during peeling is presented, with the first and last similar to those found in the present study, but the second and third are quite different due to the different interactive force. For deflection control, a sudden transition in shape is exhibited for some cases, as in the present study.

A paper by Sasaki et al. (2010) analyzes lifting of the free edge of a graphene sheet by a vertical force, with a van der Waals interactive force between the sheet and the substrate. Shapes during peeling are similar to those found here for an elastica, and, under deflection control, the force increases just before complete detachment, as here.

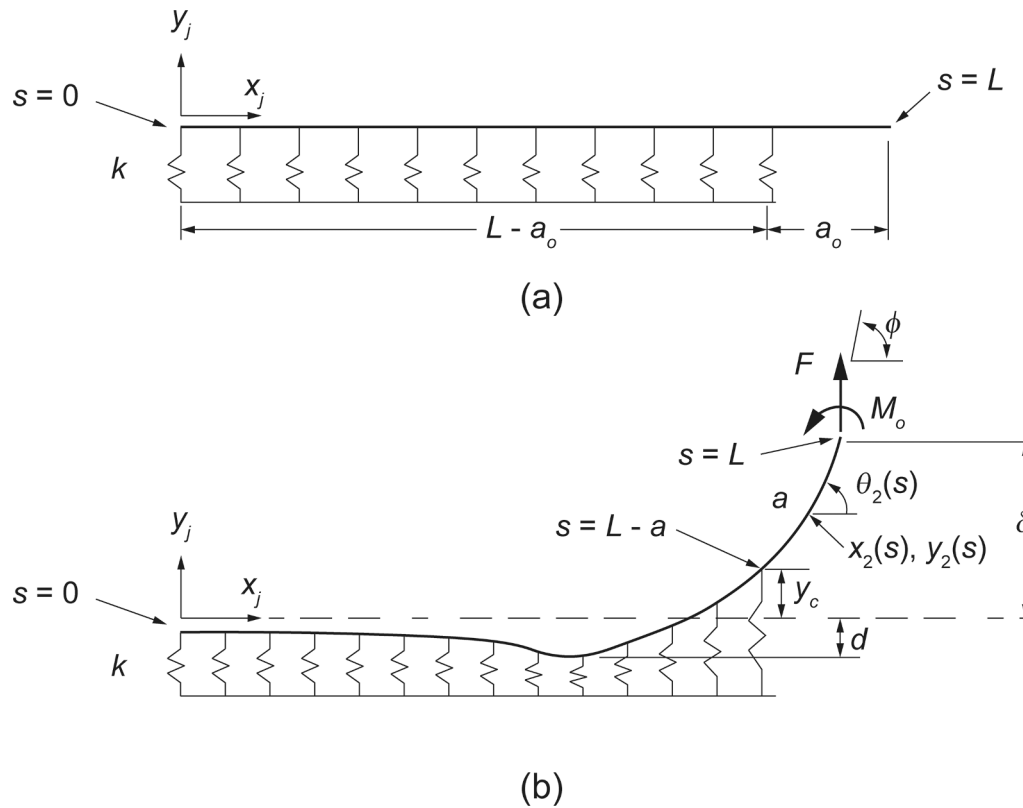Some papers consider an elastica (modeling a carbon nanotube) in

---

Fig. 1. Schematics of the elastica: (a) unloaded; (b) loaded.

which the rotation at the loaded end is fixed as the end moves upward (related to attachment to an atomic force microscope), with a van der Waals (or similar) interactive force. They include Sasaki et al. (2008; 2010), Strus et al. (2008; 2009), and Fu and Zhang (2011). Sasaki et al. (2008) and Strus et al. (2009) found sudden drops in the magnitude of the end force during peeling, as in the present study. Ishikawa et al. (2009) and Baji et al. (2015) also observed sudden changes in the force, including just before complete detachment, as here. Finally, Mead et al. (2018) tested peeling of a nanowire, with the loaded end remaining horizontal.

The analysis is formulated in Section 2. Numerical results are presented in Section 3 for deflection control and in Section 4 for rotation control. Experiments are described in Section 5, followed by concluding remarks in Section 6.

2. Formulation

Consider a thin, flexible, inextensible, unshearable, uniform, linearly elastic beam with length L, bending stiffness (flexural rigidity) EI, cross-sectional area A, weight per unit length W, and rectangular cross section having width b. As seen in Fig. 1, where $W = 0$, the arc length is s, with $s = 0$ at the left end and $s = L$ at the right (controlled) end. The initial unstrained beam is shown in Fig. 1(a) and the deformed beam is sketched in Fig. 1(b). The horizontal distance between the ends of the beam in Fig. 1(b) is not specified in the analysis, and ranges from L initially (Fig. 1(a)) to zero when the beam is vertical just before complete detachment.

The length of the unbonded portion of the beam is a, which is equal to a_0 before loading is applied. Therefore the peel front is at $s = L - a$. The horizontal and vertical coordinates are $x_j(s)$ and $y_j(s)$, respectively, and the rotation from the horizontal (in radians) is $\theta_j(s)$, where $j = 1$ for

$0 \leq s \leq L - a$ and $j = 2$ for $L - a \leq s \leq L$. The bending moment is $M_j(s)$. On the positive face of the beam cross section at s, $M_j(s)$ is positive if counter-clockwise and the vertical internal force component $Q_j(s)$ is positive if downward. The horizontal force component is zero.

The vertical deflection at the peel front $s = L - a$ is denoted y_c, the vertical deflection at the right end $s = L$ is δ, and the rotation at the right end is ϕ. Positive senses for quantities are shown in Fig. 1(b).

Displacement control is considered. At the right end ($s = L$), there is either (i) deflection control, in which the vertical end deflection δ is increased monotonically and quasi-statically (with an associated vertical force F), or (ii) rotation control, in which the end rotation ϕ is increased monotonically and quasi-statically (with an associated end moment M_0), as shown in Fig. 1(b).

The beam is modeled as an inextensible elastica, so that the bending moment is proportional to the curvature at each location. This allows large deflections and rotations. In some previous studies (e.g., Spies, 1953; Yin et al., 2020; Heide-Jørgensen et al., 2021), the unbonded segment is treated as an elastica and a linear analysis (e.g., Euler-Bernoulli theory) is applied to the rest of the beam. This would not be appropriate here, where the beam rotations can become large in the bonded segment.

The beam is attached to a Winkler foundation, consisting of a continuous distribution of vertical, independent, linearly elastic springs. The foundation stiffness is k, with the vertical restoring force per unit arc length at s being $ky(s)$ (Vaz et al., 2007). (In Nicolau and Huddleston (1982) and Panayotounakos (1989), the foundation stiffness is assumed to furnish the restoring force $ky(s)$ per unit horizontal projection instead.) Where the beam is bonded to the foundation, the work of adhesion is γ (with units of force per length).

The governing equations are (Plaut and Virgin, 2010; 2014; Yin et al., 2020)

$$\frac{dx_j}{ds} = \cos\theta_j,$$

$$\frac{dy_j}{ds} = \sin\theta_j,$$

$$EI\frac{d\theta_j}{ds} = M_j,$$

$$\frac{dM_j}{ds} = Q_j\cos\theta_j \quad (j = 1, 2),$$

$$\frac{dQ_1}{ds} = -W - ky_1,$$

$$Q_2 = (L - s)W - F.$$

$$(1)$$

The boundary conditions at $s = 0$ and $s = L$, and the transition (matching) conditions at $s = L–a$, are given by

$$s = 0 : M_1 = 0, Q_1 = 0;$$

$$s = L - a : x_1 = x_2, y_1 = y_2, \theta_1 = \theta_2, M_1 = M_2, Q_1 = Q_2;$$

$$s = L : y_2 = \delta, M_2 = M_0, Q_2 = -F.$$

$$(2)$$

The bonded arc length is written as $c = L - a$, and the total energy is given by

$$\Pi = \frac{EI}{2}\int_0^c (\theta_1')^2 ds + \frac{EI}{2}\int_c^L (\theta_2')^2 ds - \gamma bc - F\delta - M_0\theta_2(L) + \frac{1}{2}k\int_0^c y_1^2 ds + W$$

$$\times \int_0^c y_1 ds + W\int_c^L y_2 ds.$$

$$(3)$$

Stationarity of the total energy with respect to c leads to the transversality (debonding) condition

$$y_c^2 = \frac{2\gamma b}{k}.$$

$$(4)$$

Since displacement control is considered, the terms $–F\delta –M_0\theta_2(L)$ in the total energy have not been included in the derivation of Eq. (4) (Maugis, 2000; Nadler and Tang, 2008; Wang and Li, 2010). Eqs. (1), (2), and (4) are utilized in the solution procedure.

It follows from Eq. (4) that peeling (debonding) occurs when the foundation reaches the critical elongation y_c. The condition of a critical foundation elongation was previously adopted in Nicholson (1977), Plaut et al. (2001), Bernard et al. (2008), and Maddalena et al. (2009).

At the instant that the inextensible elastica detaches completely from the foundation under quasi-static conditions, the beam will be straight and vertical, with $\delta = L + y_c$. If dynamic effects were considered, complete detachment may occur earlier during the peeling process.

A shooting method is used to obtain numerical solutions of a nondimensional version of the boundary value problem. The subroutines NDSolve and FindRoot in Mathematica are utilized. An origin is placed on the beam at the peel front ($s = L–a$). One set of horizontal and vertical axes is defined for the unbonded beam to the right, and another for the bonded beam to the left, as in Plaut et al. (2001). Unknown quantities at this origin are varied until the boundary conditions at the left and right ends of the beam are satisfied with sufficient accuracy.

The characteristic length is defined as $1/\lambda$, where λ is defined by (Hétényi, 1946; Dillard et al., 2018)

$$\lambda = \left(\frac{k}{4EI}\right)^{1/4}.$$

$$(5)$$

Results will be presented in terms of nondimensional quantities such as $\gamma\lambda^2 b/k$, a/L, λL, $\lambda\delta$, λx, and λy, where y denotes y_1 for $0 \leq s \leq L–a$ and y_2 for $L–a \leq s \leq L$.

In analyses of beams attached to elastic foundations, often it is assumed that the beam is infinitely long in one direction (semi-infinite beam) or two directions from applied loads. In Fig. 1, if the beam is very long, the boundary conditions at $s = 0$ may have negligible effect on the deformation. Hétényi (1946) states that a beam can usually be treated as semi-infinite (and called a "long beam") if $\lambda L > \pi$. If $\lambda L < \pi /4 = 0.785$, a "short beam," he says that bending deformation can be neglected (i.e., the beam can be assumed to be straight). For "medium beams," with $\pi/4 < \lambda L < \pi$, he says that no such approximations should be made. It is claimed that errors will be a few percent if these long-beam and short-beam approximations are adopted. For greater accuracy, he suggests that the range for medium beams be increased to $0.60 < \lambda L < 5.00$. Seely and Smith (1952) state that a beam can be treated as semi-infinite (i.e., a long beam) if $\lambda L > 1.5\pi = 4.712$.

3. Deflection control

In this section, the beam is lifted at the right end, with associated vertical force F and with $M_0 = 0$ (Fig. 1(b)). In the numerical results in
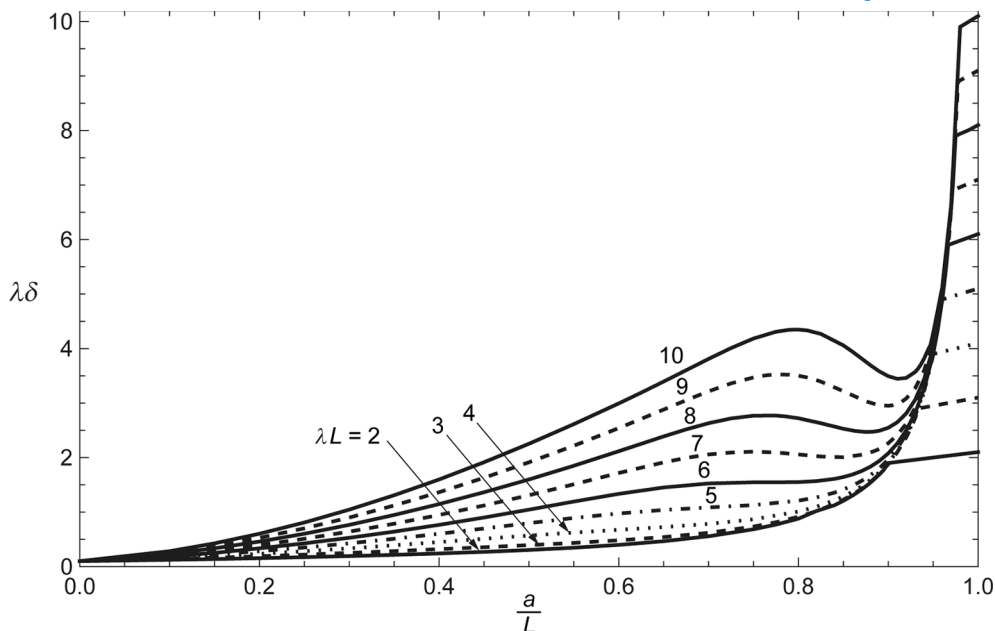

Fig. 2. Nondimensional tip deflection versus nondimensional unbonded length: $M_0 = 0$, $a_0 = 0$, $W = 0$, $\gamma\lambda^2 b/k = 0.005$.
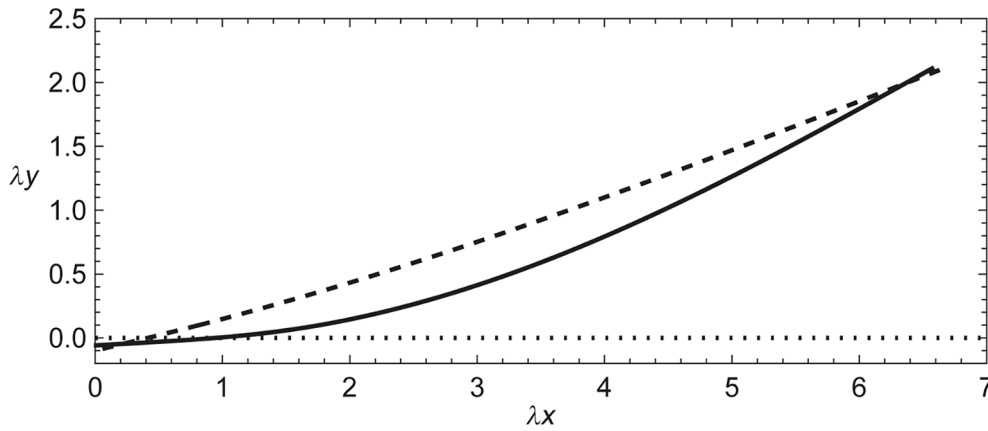
Fig. 3. Beam shapes just before transition (solid) and just after transition (dashed): $\lambda L = 7$, $M_0 = 0$, $a_0 = 0$, $W = 0$, $\gamma \lambda^2 b/k = 0.005$.

Figs. 2-13, the nondimensional work of adhesion is $\gamma \lambda^2 b/k = 0.005$ in Figs. 2-7 and 9-13 (corresponding to $\lambda y_c = 0.1$), the initial unbonded length a_0 is assumed to be zero in Figs. 2-8 and 11-13, and the self-weight W is neglected in Figs. 2-10 and 13. In other words, the effect of γ is examined in Fig. 8, the effect of a_0 in Figs. 9 and 10, and the effect of W in Figs. 11 and 12. Also, the effect of extensibility is investigated in Fig. 13.

First, the nondimensional tip deflection $\lambda \delta$ is plotted versus the nondimensional unbonded (debonded) length a/L in Fig. 2. Curves for $\lambda L = 2, 3, \ldots, 10$ are presented. Peeling is initiated (with $a/L = 0$) when $\lambda \delta = \lambda y_c$. The rightmost linear portion of each curve is associated with the beam being vertical. This portion begins at the kink located at $a/L = 1 - [2 \lambda y_c/(\lambda L)]$ where $\lambda \delta = \lambda L - \lambda y_c$, and has the formula $\lambda \delta = \lambda y_c + (a/L)\lambda L$. (For example, the kink for $\lambda L = 2$ occurs at $a/L = 0.9$ and $\lambda \delta = 1.9$.) Complete

detachment under quasi-static conditions occurs when $a/L = 1$ and $\lambda \delta = \lambda y_c + \lambda L$.

In Fig. 2, the curves for $\lambda L = 2, 3, 4,$ and 5 increase monotonically. For $\lambda L = 6, 7, 8, 9,$ and 10, however, they exhibit an internal (local) maximum followed by an internal minimum. With deflection control, in which the tip deflection δ is increased monotonically, when a maximum point is reached, the beam shifts from one configuration to another. For $\lambda L = 7$, this change in shape is depicted in Fig. 3. The solid beam shape is associated with the maximum point in Fig. 2, with $a/L = 0.748$, $F/(EI\lambda^2) = 0.027$, and $\lambda \delta = 2.109$. The dashed beam shape in Fig. 3 corresponds to $a/L = 0.883$, $F/(EI\lambda^2) = 0.007$, and again $\lambda \delta = 2.109$. The peel front is at nondimensional deflection $\lambda y = 0.1$.

If dynamic effects were considered, inertia may cause the beam to continue to debond and to completely detach from the foundation, and
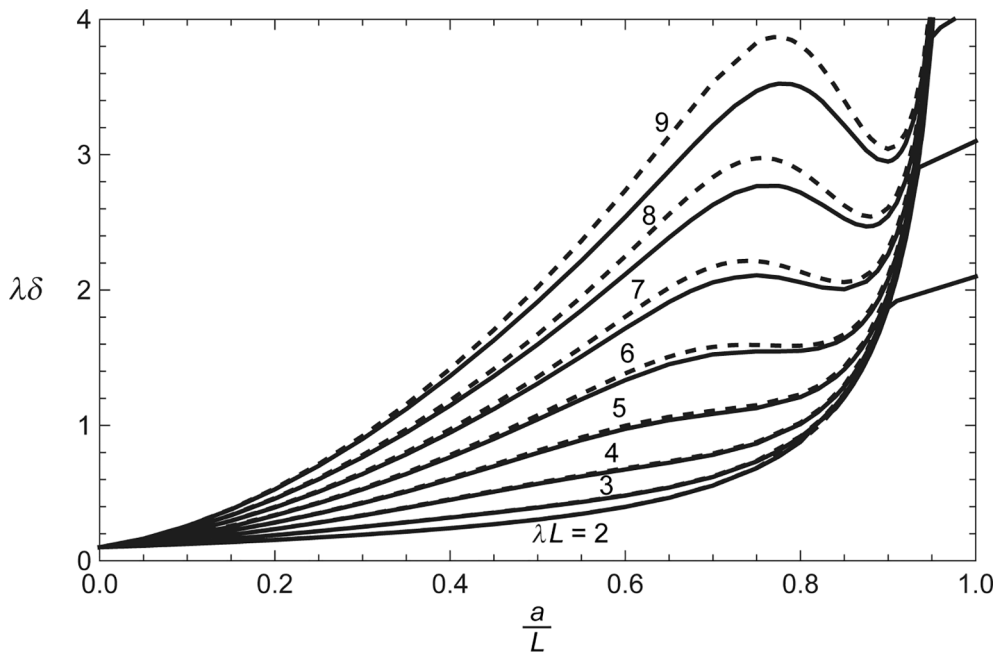

Fig. 4. Nondimensional tip deflection versus nondimensional unbonded length: $M_0 = 0$, $a_0 = 0$, $W = 0$, $\gamma \lambda^2 b/k = 0.005$; elastica (solid), Euler-Bernoulli beam theory (dashed).

then the value of δ at the internal maximum for $\lambda L = 6, 7, 8, 9$, and 10 in Fig. 2 would be a "critical" value.

In Fig. 4, with the vertical axis ending at $\lambda\delta = 4$, curves for λL from 2 to 9 in Fig. 2 are plotted as solid curves. For comparison, results from linear (Euler-Bernoulli) beam theory are plotted as dashed curves. As expected, the two sets of curves are close when displacements are small, and deviate significantly when displacements are not small. On the right part of the graph, the dashed curves do not exhibit a kink but continue upward.

For the linear theory, the deflections are $y_1(x)$ for $0 \le x \le L{-}a$ and $y_2(x)$ for $L{-}a \le x \le L$. Assume $W = 0$. The governing equilibrium equations are (Hetényi, 1946; Kinloch et al., 1994; Dillard et al., 2018)

$$EI y_1'''' + k y_1 = 0, \quad EI y_2'''' = 0 \tag{6}$$

where primes denote derivatives with respect to x. The general solution for $y_1(x)$ is listed in Dillard et al. (2018), and the general solution for $y_2(x)$ is a cubic polynomial. The boundary conditions at $x = 0$ and $x = L$, and the transition conditions at $x = L{-}a$, are given by

$$x = 0 : y_1'' = 0, y_1''' = 0;$$

$$x = L - a : y_1 = y_2, y_1' = y_2', y_1'' = y_2'', y_1''' = y_2''';$$

$$x = L : y_2 = \delta, EI y_2'' = M_0, EI y_2''' = -F. \tag{7}$$

During debonding, Eq. (4) is satisfied at $x = L{-}a$. The dashed curves in Fig. 4 are obtained by applying Eqs. (4) and (7) to the general solutions.

Equilibrium paths (force versus deflection) are presented in Fig. 5 in nondimensional terms for $\lambda L = 2, 3, 4, 5, 6, 7$, and 10. As the loaded tip of the beam is initially pulled upward, no peeling occurs until $\lambda\delta = \lambda y_c = 0.1$, and the initial curves from the origin in Fig. 5 are almost linear. The maximum value of F occurs in Fig. 5 (and in most cases in this paper) at the initiation of peeling.

For $\lambda\delta > 0.1$ and for $\lambda L > 3$, the initial portions of the curves after debonding begins are very similar. For example, the curves for $\lambda L = 6$ and 10 are almost the same from $\lambda\delta = 0.1$ to $\lambda\delta = 1.2$.

For $\lambda L \ge 6$, the equilibrium paths exhibit two vertical tangents. If $\lambda L = 7$ in Fig. 5, the upper one occurs at $\lambda\delta = 2.109$ and, under deflection control, $F/(EI\lambda^2)$ then shifts from 0.0272 to 0.0067, corresponding to the change of beam shape in Fig. 3.

For all values of λL, the equilibrium curves exhibit a bump just prior to complete detachment at $\lambda\delta = \lambda L + \lambda y_c$, associated with a vertical equilibrium shape. This is seen for $\lambda L = 2$ in Fig. 5. The formula for the bump, having the range $\lambda L - \lambda y_c \le \lambda\delta \le \lambda L + \lambda y_c$, is

$$\frac{F}{EI\lambda^2} = 2\left[(\lambda y_c)^2 - (\lambda L - \lambda\delta)^2\right]. \tag{8}$$

For $\lambda L = 3$, a sequence of beam shapes is shown in Fig. 6 for $a/L = 0.1, 0.3, 0.5, 0.7, 0.8, 0.9$, and 0.95 (vertical beam). The corresponding values of $F/(EI\lambda^2)$, respectively, are 0.152, 0.096, 0.054, 0.020, 0.009, 0.002, and 0.015, with $\lambda\delta = 0.138, 0.251, 0.393, 0.619, 0.914, 1.877$, and 2.95.

In Fig. 7, the associated nondimensional vertical force is plotted versus the nondimensional unbonded length for $\lambda L = 2, 4, 6, 8$, and 10. The curves for $\lambda L = 4, 6, 8$, and 10 are wavy. For a given value of a/L, the force is not monotonic as λL increases from 2 to 10. As a/L approaches unity (complete detachment), each curve exhibits a bump having the range $1{-}[2 \lambda y_c/(\lambda L)] \le a/L \le 1$ and given by

$$\frac{F}{EI\lambda^2} = 2(\lambda L - \lambda a)(\lambda a + 2\lambda y_c - \lambda L). \tag{9}$$

In Eq. (9), λa can be written as $(a/L)\lambda L$.

The effect of the work of adhesion on the vertical force at the initiation of debonding, denoted F_{max}, is considered in Fig. 8, where the curves are associated with $\gamma\lambda^2 b/k = 0.00125, 0.005, 0.01125$, and 0.020 (corresponding to $\lambda y_c = 0.05, 0.10, 0.15$, and 0.20, respectively). The horizontal axis begins at $\lambda L = 0.3$. The curves are almost linear for small λL with $F_{max}/(EI\lambda^2)$ approximately equal to $(\lambda y_c)(\lambda L)$, and are
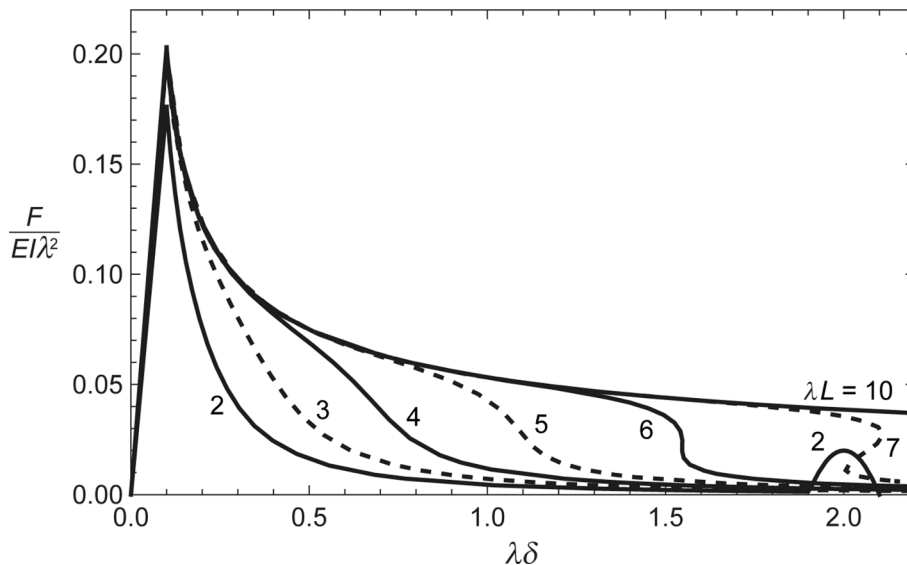

Fig. 5. Nondimensional vertical force versus nondimensional tip deflection: $M_0 = 0$, $a_0 = 0$, $W = 0$, $\gamma\lambda^2 b/k = 0.005$.
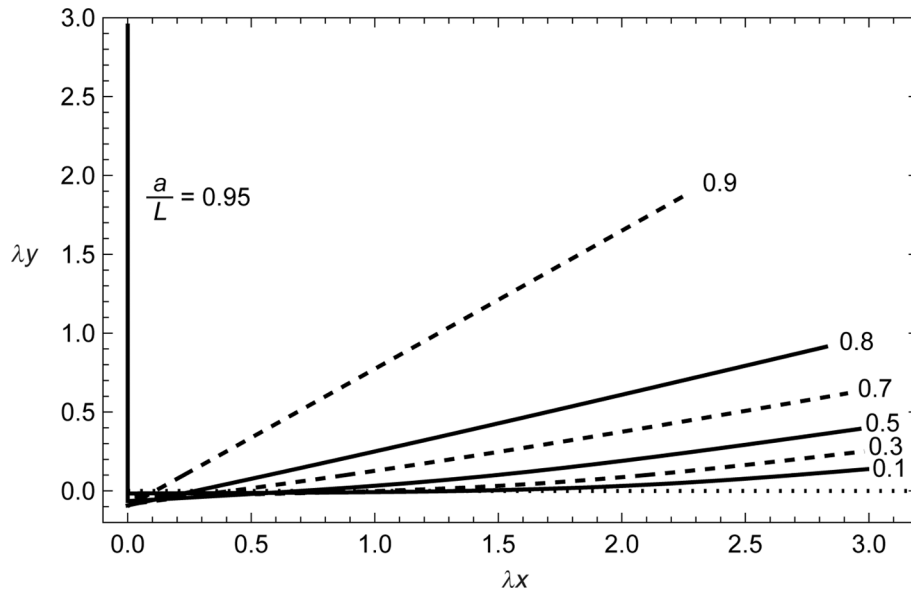
Fig. 6. Sequence of beam shapes: $\lambda L = 3$, $M_0 = 0$, $a_0 = 0$, $W = 0$, $\gamma \lambda^2 b/k = 0.005$.
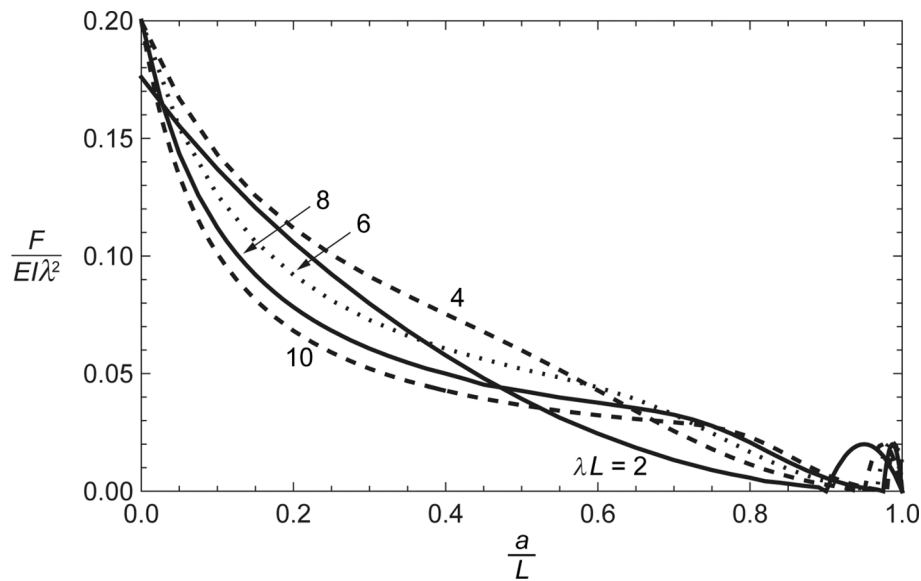

Fig. 7. Nondimensional vertical force versus nondimensional unbonded length: $M_0 = 0$, $a_0 = 0$, $W = 0$, $\gamma \lambda^2 b/k = 0.005$; $\lambda L = 2$ (solid), 4 (dashed), 6 (dotted), 8 (solid), 10 (dashed).

almost horizontal for $\lambda L > 3$ with $F_{max}/(EI\lambda^2)$ approximately equal to $2 \lambda y_c$.

If Euler-Bernoulli theory is used, Eqs. (5)-(7) with $a = M_0 = a_0 = W = 0$ lead to the formula

$$F_{max} = EI\lambda^2 \sqrt{\frac{8\gamma\lambda^2 b}{k}} \ \frac{(2 - \cos 2\lambda L - \cosh 2\lambda L)}{(\sin 2\lambda L - \sinh 2\lambda L)} \qquad (10)$$

It is noted that when $\gamma\lambda^2 b/k$ is fixed in a figure, and λ is a factor associated with the curves and/or one or both axes, then the dimensional value γ changes if one considers λ to change.

The effect of an initial unbonded length a_0 (see Fig. 1(a)) is presented in Figs. 9 and 10, and was previously considered in Peng et al. (2019), Yin et al. (2020), Heide-Jørgensen et al. (2021), and Wan et al. (2021) for peeling, and in Bidokhti et al. (2017) for a double cantilever beam

test, among others. In Fig. 9, the nondimensional vertical force is plotted versus the nondimensional tip deflection for $\lambda L = 3$, $\gamma\lambda^2 b/k = 0.005$, and $a_0/L = 0$, 0.1, 0.2, 0.3, 0.4, and 0.5. The dashed curves correspond to the behavior before peeling is initiated. The result for $a_0 = 0$ was included in Fig. 5 with a different range on the horizontal axis. For $a_0/L = 0$, 0.1, 0.2, 0.3, 0.4, and 0.5, respectively, peeling begins when $\lambda\delta = 0.100$, 0.138, 0.189, 0.251, 0.319, and 0.393, and $F_{max}/(EI\lambda^2) = 0.199$, 0.152, 0.121, 0.096, 0.075, and 0.054.

As a_0 increases, the slope of the dashed curve decreases and the maximum force F_{max} decreases, as for similar problems treated in Peng et al. (2019) and Yin et al. (2020). The effect of λL on F_{max} is depicted in Fig. 10 for the same values of a_0/L, with the horizontal axis beginning at $\lambda L = 0.5$. The curve for $a_0/L = 0$ was included in Fig. 8 with different scales on the axes. For the curves in Fig. 10 with $a_0/L > 0$, as λL increases, F_{max} initially increases and then decreases, which is quite different from the monotonic behavior when $a_0 = 0$. It is also noted that
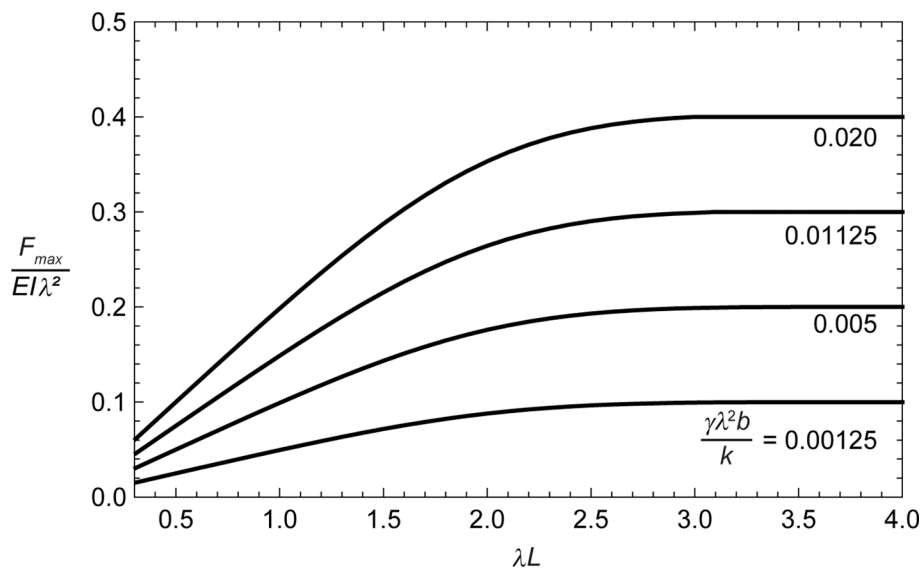
Fig. 8. Nondimensional maximum vertical force versus nondimensional beam length: $M_0 = 0$, $a_0 = 0$, $W = 0$; $\gamma\lambda^2 b/k = 0.00125, 0.005, 0.01125, 0.020$ ($\lambda y_c = 0.05$, 0.10, 0.15, 0.20).
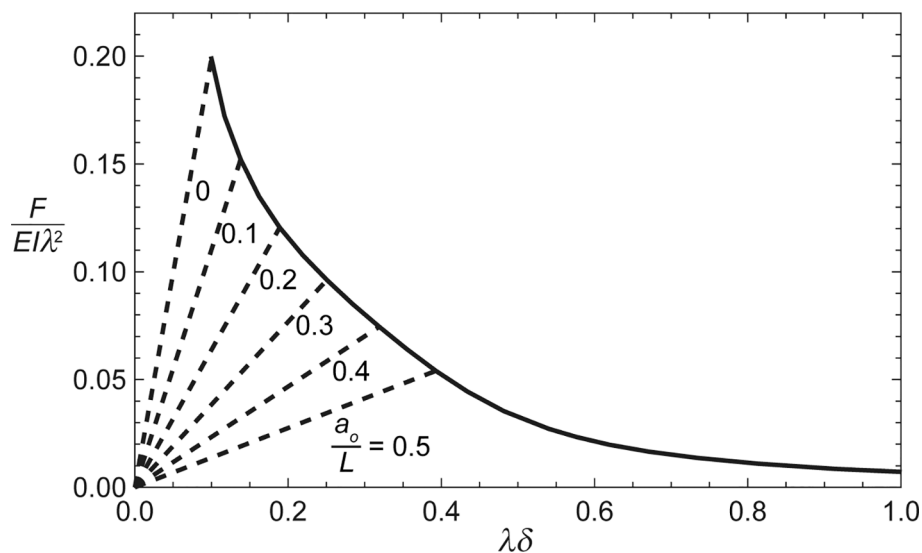

Fig. 9. Nondimensional vertical force versus nondimensional tip deflection: $\lambda L = 3$, $M_0 = 0$, $W = 0$, $\gamma\lambda^2 b/k = 0.005$.
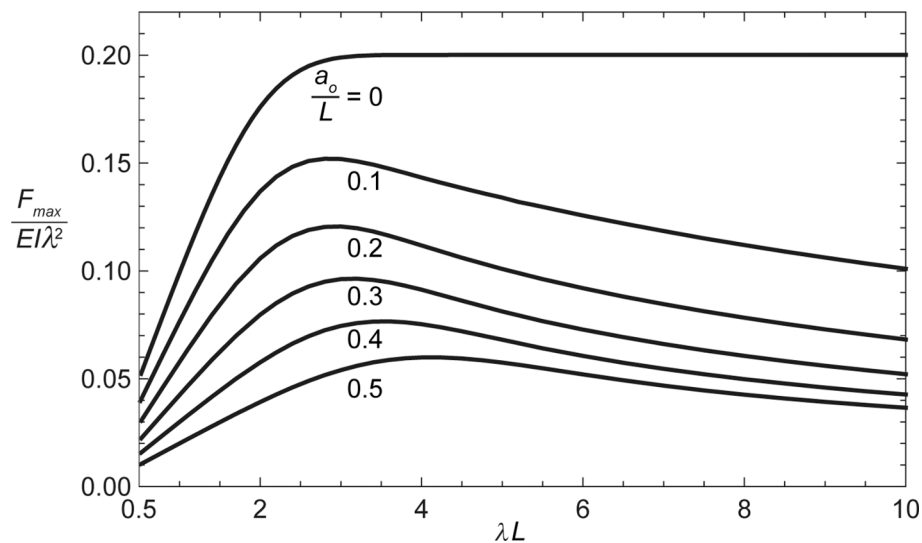

Fig. 10. Nondimensional maximum vertical force versus nondimensional beam length: $M_0 = 0$, $W = 0$, $\gamma\lambda^2 b/k = 0.005$.

on those curves, if L increases as λL increases, then a_0 increases correspondingly.

The effect of the beam's self-weight W is examined next. (Iandiorio and Salvini (2020; 2022), including self-weight, examined lifting of an elastica from a rigid foundation by an end force and moment, with no adhesion.) Results are presented in Figs. 11 and 12, with $\lambda L = 3$, $a_0 = 0$, and $\gamma\lambda^2 b/k = 0.005$.

In Fig. 11, the nondimensional tip deflection $\lambda\delta$ is plotted versus the nondimensional unbonded length a/L for $W/(EI\lambda^3) = 0$, 0.05, and 0.1. The curve for $W = 0$ was included in Figs. 2 and 4. The value of a/L at the kink, where the beam becomes vertical, is

$$\frac{a}{L} = 1 - \frac{\lambda y_c}{\lambda L} - \left[\left(\frac{\lambda y_c}{\lambda L}\right)^2 + \frac{1}{2\lambda L}\frac{W}{EI\lambda^3}\right]^{1/2}. \tag{11}$$

The corresponding value of $\lambda\delta$ is given by $\lambda y_c + (a/L)\lambda L$.

Before the kink, at a given value of a/L, the tip deflection increases as W increases. The maximum downward deflection d of the bottom end of the vertical beam into the elastic foundation (see Fig. 1(b)) is given by

$\lambda d = 0.10$, 0.29, and 0.40 for $W/(EI\lambda^3) = 0$, 0.05, and 0.1, respectively,

In Fig. 12, the nondimensional vertical force is plotted versus the nondimensional unbonded length a/L, again for $W/(EI\lambda^3) = 0$, 0.05, and 0.1. The value of a/L at the kink is given by Eq. (11). Past the kink, the value of the force is given by

$$\frac{F}{EI\lambda^2} = \frac{\lambda LW}{EI\lambda^3} + 2(\lambda L - \lambda a)(\lambda a + 2\lambda y_c - \lambda L). \tag{12}$$

Eq. (12) can be obtained by equilibrium of the vertical beam when length y_c above the foundation level is pulled downward by the foundation and length $(L-a-y_c)$ below the foundation is pushed upward by the foundation. The associated peak value of the force, F_{peak}, occurs at $a/L = (\lambda L-\lambda y_c)/(\lambda L)$, which is independent of W, and is given by

$$\frac{F_{peak}}{EI\lambda^2} = \frac{\lambda LW}{EI\lambda^3} + 2(\lambda y_c)^2. \tag{13}$$

At complete detachment ($a/L = 1.0$), the force F equals the total weight of the beam. For example, in Fig. 12, if the normalized self-weight is 0.1 (with the normalized beam length being 3), then the
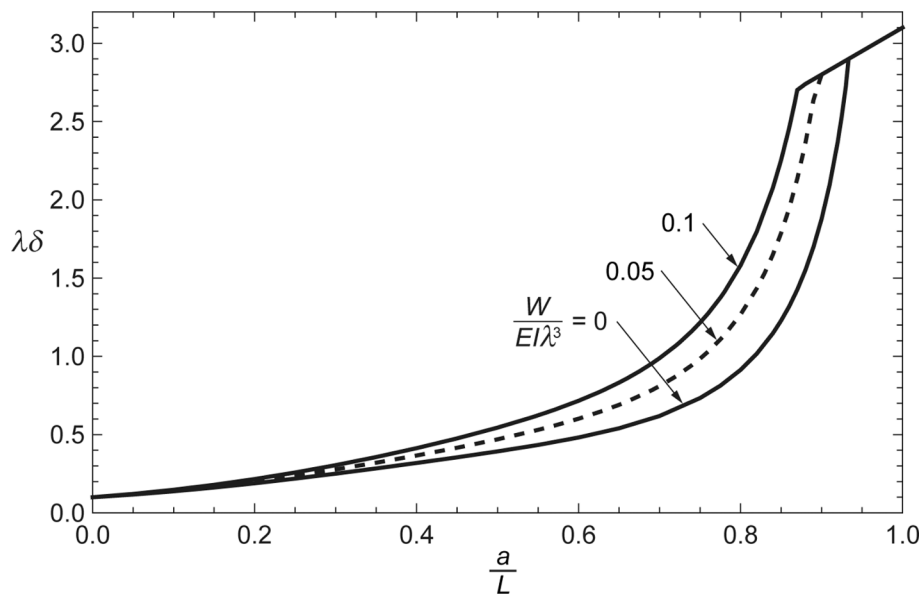

Fig. 11. Nondimensional tip deflection versus nondimensional unbonded length: $\lambda L = 3$, $M_0 = 0$, $a_0 = 0$, $\gamma\lambda^2 b/k = 0.005$.
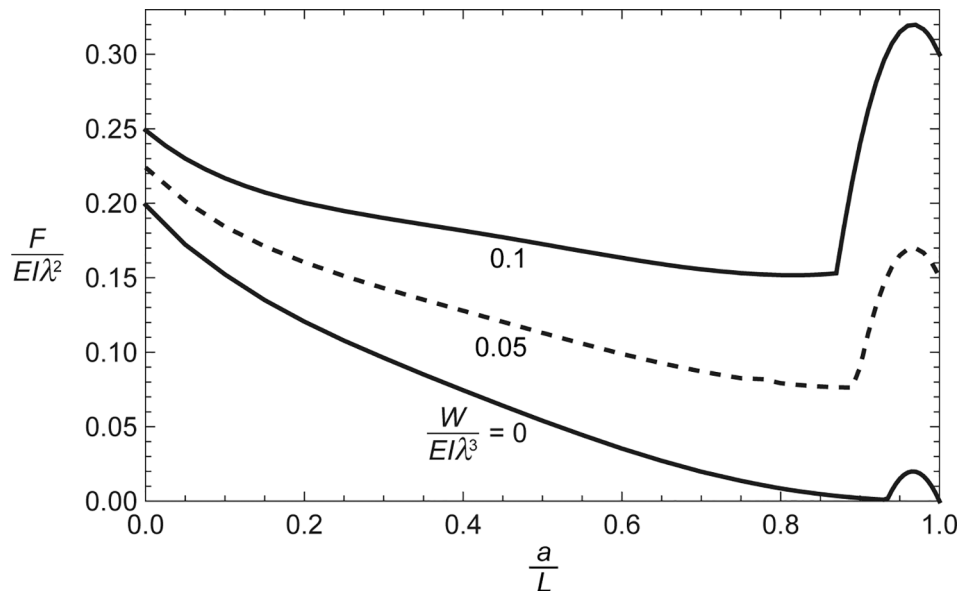

Fig. 12. Nondimensionl vertical force versus nondimensional unbonded length: $\lambda L = 3$, $M_0 = 0$, $a_0 = 0$, $\gamma\lambda^2 b/k = 0.005$.
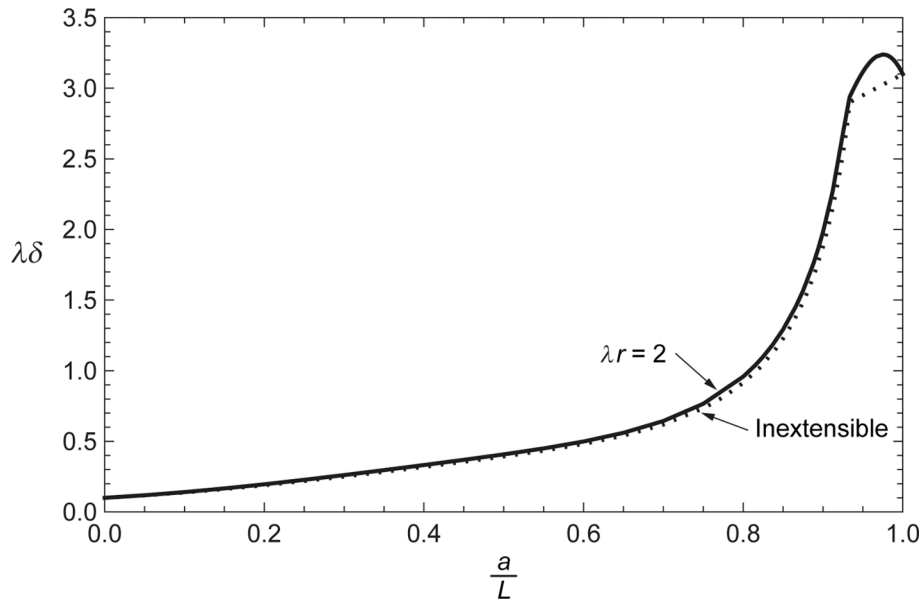
Fig. 13. Nondimensional tip deflection versus nondimensional unbonded length: $\lambda L = 3$, $M_0 = 0$, $a_0 = 0$, $W = 0$, $\gamma\lambda^2 b/k = 0.005$; inextensible (dotted), extensible with $\lambda r = 2$ (solid).

curve has the value 0.1×3 at the right end.

For the top curve in Fig. 12, the maximum value of the force during peeling does not occur when peeling is initiated, but just before complete detachment, and can be computed from Eq. (13).

The effect of extensibility of the elastica is considered now. The axial strains are denoted ε_1 for $0 < s < L-a$, and ε_2 for $L-a < s < L$. They are given by

$$\varepsilon_1 = -\frac{Q_1\sin\theta_1}{EA}, \varepsilon_2 = \frac{F\sin\theta_2}{EA}. \tag{14}$$

In Eq. (1), a new factor $(1 + \varepsilon_1)$ is included on the right sides of the equations for dx_1/ds, dy_1/ds, and dM_1/ds, and a new factor $(1 + \varepsilon_2)$ is included on the right sides of the equations for dx_2/ds, dy_2/ds, and dM_2/ds (Plaut, 2010; Chen and Tsao, 2013).

The radius of gyration r, and the equation of λr for a beam with rectangular cross section of width b and depth h, are respectively

$$r = \sqrt{\frac{I}{A}}, \quad \lambda r = \frac{1}{2}\left(\frac{kh}{3Eb}\right)^{1/4}. \tag{15}$$

In Fig. 13, with $\lambda L = 3$, the nondimensional tip deflection is plotted versus the nondimensional unbonded length for the extensible case $\lambda r = 2$ (solid curve) and for the inextensible elastica ($\varepsilon_1 = \varepsilon_2 = \lambda r = 0$). For $\lambda r = 2$ in Fig. 13, the maximum axial strain is 0.08 and occurs at the loaded end of the beam when peeling begins ($a/L = 0$), and the minimum axial strain is –0.08 and occurs at the center of the small bonded part when $a/L = 0.93$. Higher values of λr lead to higher strain magnitudes.

For both curves in Fig. 13, the beam becomes vertical when $a/L = 0.933$, given by Eq. (11). For the extensible case (solid curve), a maximum occurs at $a/L = 0.975$ and $\lambda\delta = 3.239$. Under deflection control, when this maximum point is reached, apparently the beam will jump off the substrate dynamically.

4. Rotation control

In this section, a counter-clockwise rotation ϕ is applied to the right
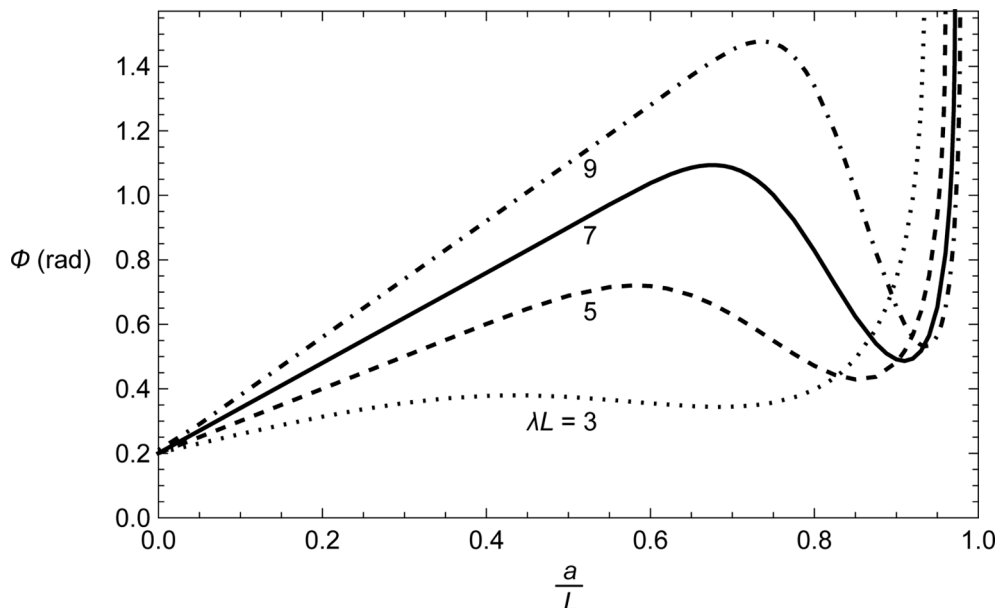

Fig. 14. End rotation versus nondimensional unbonded length: $F = 0$, $a_0 = 0$, $W = 0$, $\gamma\lambda^2 b/k = 0.005$.
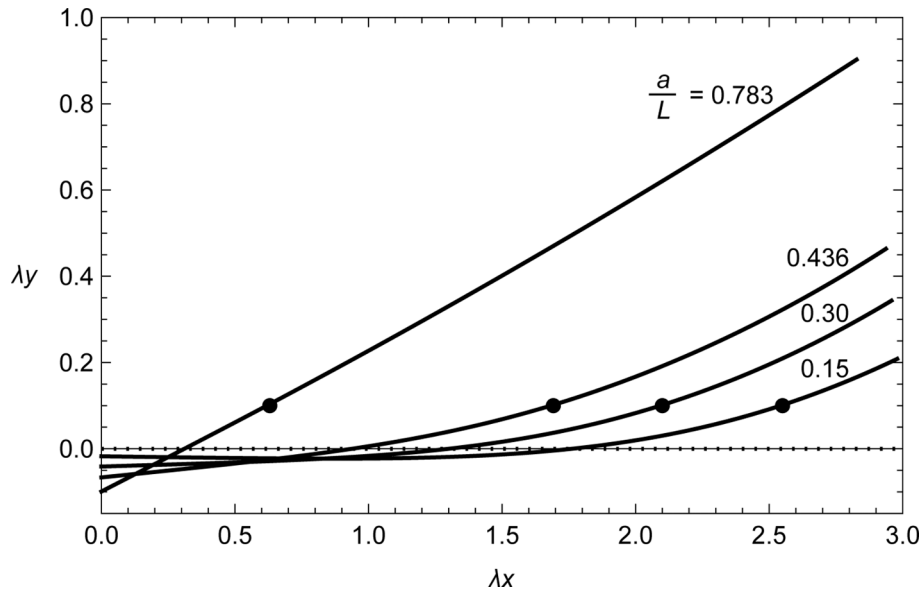
Fig. 15. Sequence of beam shapes: $\lambda L = 3$, $F = 0$, $a_0 = 0$, $W = 0$, $\gamma \lambda^2 b/k = 0.005$.
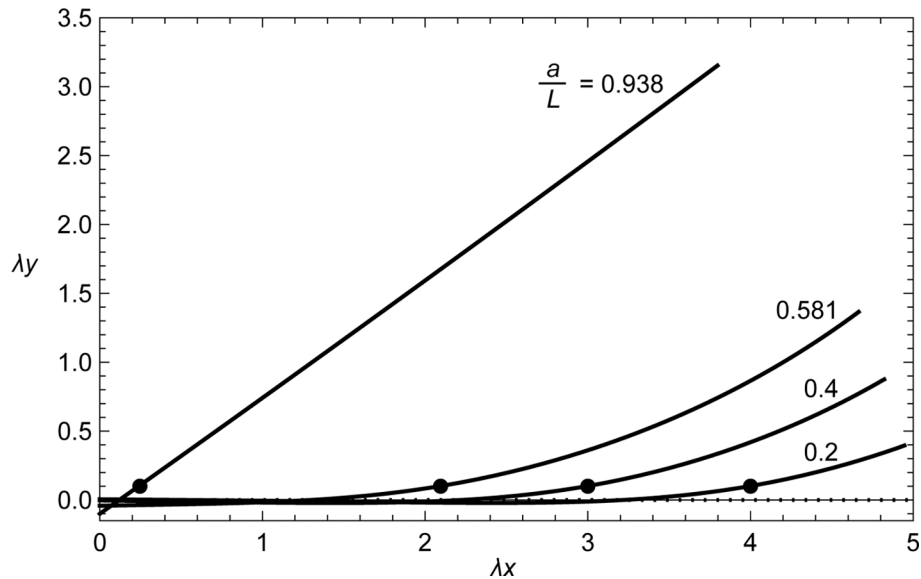

Fig. 16. Sequence of beam shapes: $\lambda L = 5$, $F = 0$, $a_0 = 0$, $W = 0$, $\gamma \lambda^2 b/k = 0.005$.

end of the inextensible elastica, with $F = 0$ (Fig. 1(b)). The associated end moment is M_0. In the numerical examples, $\gamma \lambda^2 b/k = 0.005$ ($\lambda y_c = 0.1$), $a_0 = 0$, and $W = 0$. Peeling caused by an applied end moment was previously studied by Cotterell et al. (2006) and Iandiorio and Salvini (2020; 2022). The unbonded segment of the beam has constant curvature (i.e., is circular).

The end rotation ϕ is plotted versus the nondimensional unbonded length a/L in Fig. 14 for $\lambda L = 3$, 5, 7, and 9. The curves exhibit an internal maximum and internal minimum, and ϕ becomes large as a/L approaches unity. In the plots involving ϕ in this section, $0 \leq \phi \leq \pi/2$. For $\lambda L = 3$, 5, 7, and 9, respectively, the maxima occur at $a/L = 0.436$, 0.581, 0.676, and 0.737, and have the values $\phi = 0.380$, 0.721, 1.094, and 1.478 rad. When the maximum point is reached, the beam may transition to the equilibrium configuration with $a/L = 0.783$, 0.938, 0.968, and 0.978 for $\lambda L = 3$, 5, 7, and 9, respectively, or the beam may detach from the foundation dynamically.

A sequence of shapes for $\lambda L = 3$ is shown in Fig. 15. Dots denote the locations of the peel front. For $a/L = 0.15$, 0.30, 0.436 (the location of

the internal maximum in Fig. 14), and 0.783, respectively, the end deflection is $\lambda \delta = 0.208$, 0.343, 0.464, and 0.903. When the internal maximum in Fig. 14 is reached, the beam may shift to the almost-linear equilibrium shape for $a/L = 0.903$ shown in the figure and having the same end rotation as for $a/L = 0.436$.

A sequence of shapes for $\lambda L = 5$ is shown in Fig. 16. For $a/L = 0.2$, 0.4, 0.581 (at the internal maximum in Fig. 14), and 0.938, respectively, $\lambda \delta = 0.395$, 0.876, 1.365, and 3.153. The curves are similar in form to those in Fig. 14.

Fig. 17 illustrates the variation of the associated nondimensional end moment $M_0/(\lambda EI)$ versus the nondimensional unbonded length, with $\lambda L = 3$, 4, 5, 7, and 9. As peeling begins, the end moment remains almost constant for a range of a/L that increases as λL increases, and then the end moment decreases to zero. The forms of the curves in Fig. 17 are quite different from those in Fig. 7 for deflection control.

Finally, in Fig. 18, the nondimensional end moment is plotted versus the end rotation for $\lambda L = 3$, 4, 5, 7, and 9. The dashed line governs before peeling is initiated. The upper vertical tangents occur at
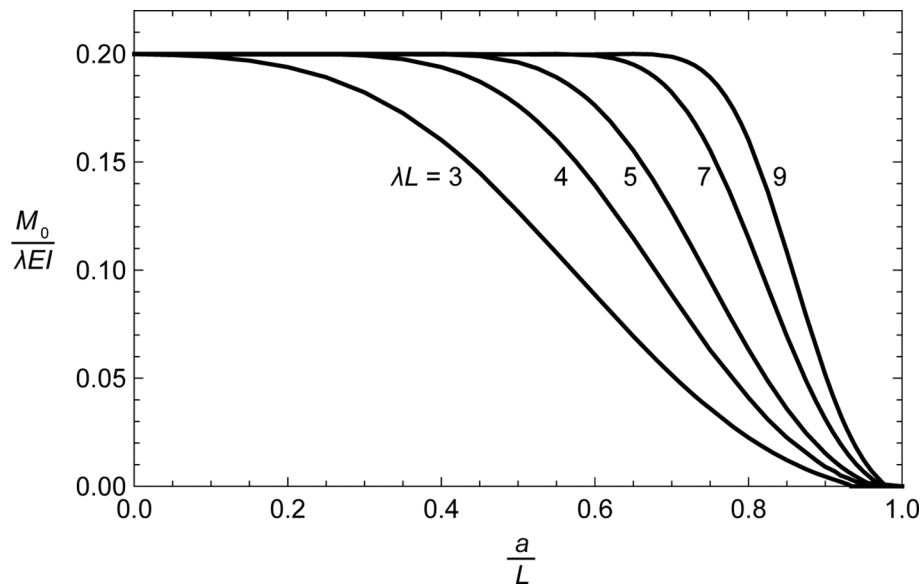
Fig. 17. Nondimensional end moment versus nondimensional unbonded length: $F = 0$, $a_0 = 0$, $W = 0$, $\gamma\lambda^2 b/k = 0.005$.
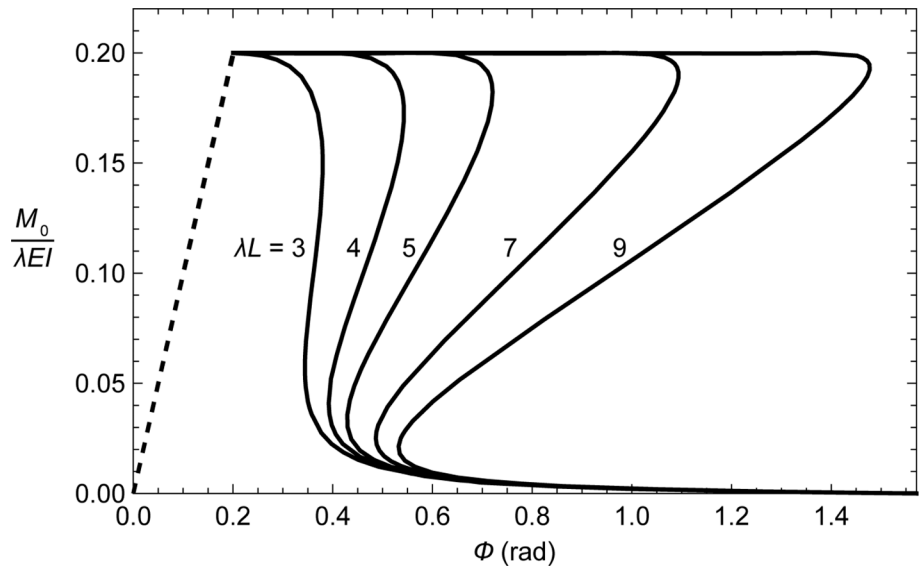

Fig. 18. Nondimensional end moment versus end rotation: $F = 0$, $a_0 = 0$, $W = 0$, $\gamma\lambda^2 b/k = 0.005$.

$\phi = 0.380$, 0.543, 0.721, 1.094, and 1.478 rad, respectively, for $\lambda L = 3$, 4, 5, 7, and 9.

5. Experiments

The experiments were performed by bonding 0.5 mm thick, 35 mm wide beams of polyethylene terephthalate glycol (PETG) with different lengths (50, 30, 20, 15, 10, 5 mm) onto a compliant foundation. The experiments were run at a crosshead displacement rate of 25 mm/min. The foundation was an elastomeric material of thickness $h = 1.5$ mm composed of a silicone elastomer (Dow Corning Sylgard 184) mixed at a 10:1 ratio with a dispersion of polyethylenimine (PEIE) at 0.4 vol%. The PEIE modifies the crosslinking reaction of the silicone elastomer and makes the foundation more adhesive. The value G_C (i.e., γ) was measured to be 15 N/m through a 90° peel experiment at a crack velocity of 25 mm/min, and the foundation modulus was $E_a = 100$ kPa measured through uniaxial tension experiments.

Deflection control was applied. The experiment was performed on a

peel fixture by attaching one end of the beam to a vertical wire that connected to the load cell to measure the corresponding force. The wire was bonded to the PETG beam through a laser cut acrylic block that evenly distributed the load across the beam width. Fig. 19 is a photo of the experiment during lifting of a beam with length $L = 50$ mm.

The experiments show that for small values of the nondimensional λL parameter, the maximum vertical force increases with increasing λL. This occurs until approximately $\lambda L = 2$, after which the experimental maximum vertical force values plateau. This is found to show good agreement with the analysis, as shown in Fig. 20. (In the analysis, $E = 2$ GPa, $k = E_a b/h$, $\lambda = 168.2$ m^{-1}, $\lambda y_c = 0.113$, $\gamma\lambda^2 b/k = 0.00636$, $M_0 = 0$, $a_0 = 0$, and $W = 0$.).

Experimental equilibrium paths (force versus tip deflection) are presented in Fig. 21. They can be compared with those in Fig. 5. In Fig. 21, for the case $L = 10$ mm, there is a hump before complete detachment, as also seen in the theoretical results. For the case $L = 50$ mm (with $\lambda L = 8.41$), the descending curve is wavy, which is somewhat similar to the curves in Fig. 5 for $\lambda L = 5$ and 6. The curves in Fig. 21 do
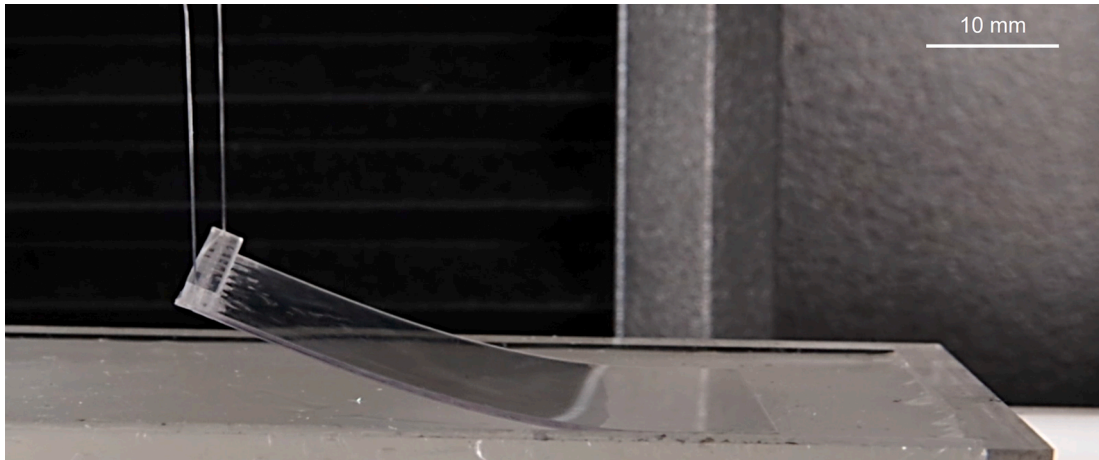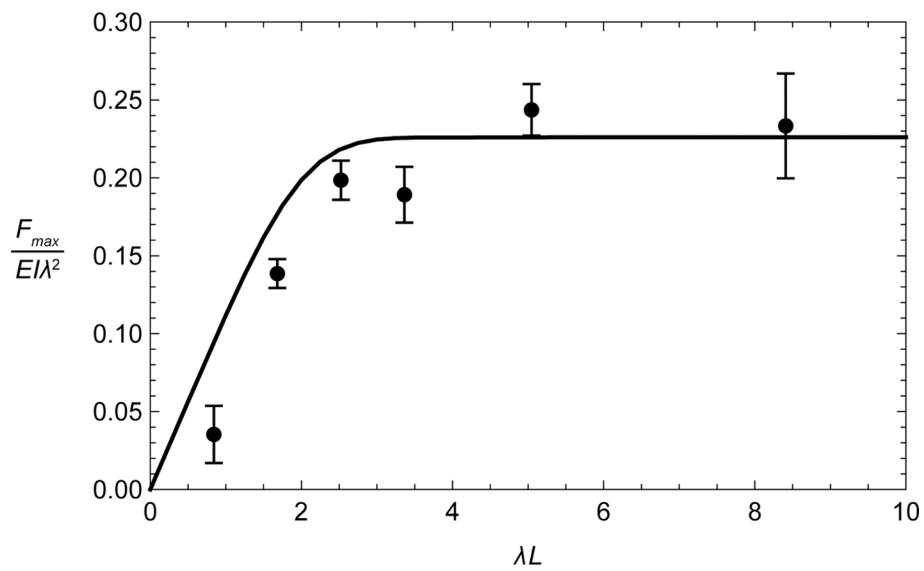
Fig. 19. Photo of experiment.

Fig. 20. Experimental comparison of the nondimensional maximum vertical force versus nondimensional beam length. The data points represent the experiments, while the error bars represent the standard deviation with $n = 3$. The solid line represents the analysis.
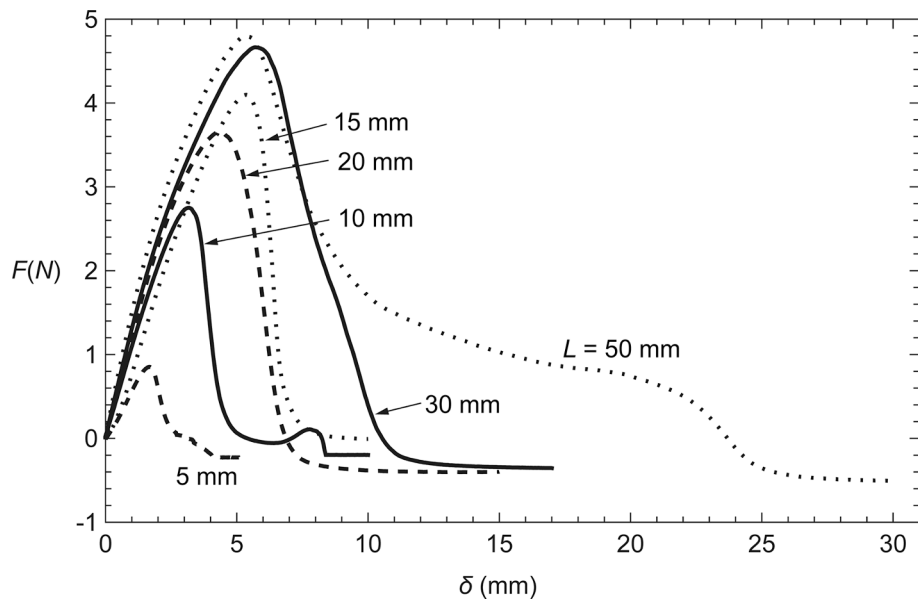

Fig. 21. Vertical force versus tip deflection from experiment for six beam lengths.

not have a sharp point at the top, but sharp cusps predicted by models are seldom realized experimentally, where slight imperfections, time-dependent effects, and other factors often tend to soften or smooth the behavior predicted by idealized models. Although we have seen catastrophic failures supporting the predicted instabilities with time-independent materials, the current PDMS adhesive exhibits some rate dependence, as seen in the gradual initial debonding that leads to departure from linear behavior, the softening of the load peak, and the more gradual and stable debonding observed for the 50-mm-long beam.

6. Concluding remarks

This paper has focused on the complete detachment of finite-length beams adhered to a substrate, using the beam-on-elastic-foundation model. Much of the previous work on peeling has considered long beams (sometimes infinite or semi-infinite) and/or steady-state (self-similar) peeling.

The horizontal, linearly elastic beam was modeled as an inextensible elastica, and was subjected either to deflection control or rotation control at one end. It was assumed that bending of the beam was more important than stretching. At the peel front, the debonding condition was obtained by fracture mechanics and corresponded to a critical vertical foundation deflection. For quasi-static behavior, the beam became vertical just before it detached. The effects of the relative foundation stiffness, the work of adhesion (and critical foundation deflection), and the length, self-weight, extensibility, and initial unbonded length of the beam were examined.

For the case of deflection control, a sudden shift in shape occurred during peeling if the nondimensional beam length λL was sufficiently large, where L is the beam length and $1/\lambda$ is its characteristic length defined in Eq. (5). Inertia could cause the beam in practice to continue debonding and completely detach from the foundation. If not, during final pulling of the vertical beam, the associated vertical force increased and then decreased. The maximum force usually occurred at the initiation of peeling; it increased with an increase in (i) λL, (ii) the work of adhesion (and critical foundation deflection), and (iii) the self-weight, and it decreased with an increase in the initial unbonded length.

For the case of rotation control, with no self-weight, the maximum associated end moment occurred at the initiation of peeling and, for sufficiently high values of λL, remained at that value during an initial phase of peeling. During peeling, the end moment decreased to zero when the beam became vertical, with part of the beam below the foundation level.

A basic Winkler foundation was considered, and therefore shear resistance of the foundation was not included. A linear (Euler-Bernoulli) beam theory was not appropriate due to the large deflections and rotations of the beam before complete detachment, although it was shown to be fairly accurate during an initial stage of peeling.

The Winkler foundation model consists of a continuous distribution of independent vertical springs. The maximum nondimensional upward deflection of the foundation in almost all of the examples in this paper is 0.1, whereas the nondimensional length of the beam is in the range 2–10 in most of the numerical results. However, the upward deflection of the foundation cannot be compared to the thickness of the foundation, which is not explicitly involved in the analysis. The linear model used for the foundation is more reliable for cases in which the maximum upward deflection of the foundation is small compared to the foundation thickness.

Peeling of a slender, flexible adherend from a substrate arises in various situations (Dillard et al., 2018; Hwang et al., 2018). Few previous studies have analyzed peeling until complete detachment occurs, but the phenomenon is of interest (e.g., Buchoux et al., 2011; Fu and Zhang, 2011; Sekiguchi et al., 2012; 2014; Wu et al., 2015; Gu et al., 2016; Peng et al., 2019; Gouravaraju et al., 2021). The behavior just before such detachment can be surprising, as demonstrated in examples here. It may require an increase in the peel force, which may be

important to know. The results presented here are new and should be useful in a variety of applications, including biological adhesion.

Declaration of Competing Interest

The authors declare that they have no known competing financial interests or personal relationships that could have appeared to influence the work reported in this paper.

Data availability

Data will be made available on request.

References

Baji, A., Zhou, L., Mai, Y.-W., Yang, Z., Yao, H., 2015. On the adhesion performance of a single electrospun fiber. Applied Physics A 118, 51–56.

Bernard, C., Marsaudon, S., Boisgard, R., Aimé, J.-P., 2008. Competition of elastic and adhesive properties of carbon nanotubes anchored to atomic force microscopy tip. Nanotechnology 19, 035709.

Bidokhti, A.A., Shahani, A.R., Fasakhodi, M.R.A., 2017. Displacement-controlled crack growth in double cantilever beam specimen: A comparative study of different models. Proceedings of the Institution of Mechanical Engineers Part C 231, 2835–2847.

Buchoux, J., Bellon, L., Marsaudon, S., Aimé, J.-P., 2011. Carbon nanotubes adhesion and nanomechanical behavior from peeling force spectroscopy. European Physical Journal B 84, 69–77.

Chen, J.-S., Tsao, H.-W., 2013. Static snapping load of a hinged extensible elastica. Applied Mathematical Modelling 37, 8401–8408.

Cotterell, B., Hbaieb, K., Williams, J.G., Hadavinia, H., Tropsa, V., 2006. The root rotation in double cantilever beam and peel tests. Mechanics of Materials 38, 571–584.

Dillard, D.A., Mukherjee, B., Karnal, P., Batra, R.C., Frechette, J., 2018. A review of Winkler's foundation and its profound influence on adhesion and soft matter applications. Soft Matter 14, 3669–3683.

Fu, Y.-M., Zhang, P., 2011. Peeling off carbon nanotubes from rigid substrates: An exact model. Journal of Adhesion Science and Technology 25, 1061–1072.

Gouravaraju, S., Sauer, R.A., Gautam, S.S., 2021. Investigating the normal and tangential peeling behaviour of gecko spatulae using a coupled adhesion-friction model. Journal of Adhesion. https://doi.org/10.1080/00218464.2020.1719838 access online 2/20.

Gu, Z., Li, S., Zhang, F., Wang, S., 2016. Understanding surface adhesion in nature: A peeling model. Advanced Science 3, 1500327.

Heide-Jørgensen, S., Budzik, M.K., Buhl, K.B., Hinge, M., Pedersen, S.U., Daasbjerg, K., Kongsfelt, M., 2021. Mode I debonding under large deformation conditions including notes on cleavage-peeling transition. Engineering Fracture Mechanics 241, 107413.

Hetényi, M., 1946. Beams on Elastic Foundation. University of Michigan Press, Ann Arbor, MI.

Hwang, D.-G., Trent, K., Bartlett, M.D., 2018. Kirigami-inspired structures for smart adhesion. ACS Applied Materials & Interfaces 10, 6747–6754.

Iandiorio, C., Salvini, P., 2020. Heavy elastica soil-supported with lifting load and bending moment applied to an end: A new analytical approach for very large displacements and experimental validation. International Journal of Solids and Structures 206, 153–169.

Iandiorio, C., Salvini, P., 2022. Inflectional heavy elastica with unilateral contact constraint: Analytical solution through the curvilinear abscissa mapping approximation. International Journal of Solids and Structures 234–235, 111258.

Ishikawa, M., Harada, R., Sasaki, N., Miura, K., 2009. Adhesion and peeling forces of carbon nanotubes on a substrate. Physical Review B 80, 193406.

Kinloch, A.J., Lau, C.C., Williams, J.G., 1994. The peeling of flexible laminates. International Journal of Fracture 66, 45–70.

Maddalena, F., Percivale, D., Puglisi, G., Truskinovsky, L., 2009. Mechanics of reversible unzipping. Continuum Mechanics and Thermodynamics 21, 251–268.

Maugis, D., 2000. Contact, Adhesion and Rupture of Elastic Solids. Springer-Verlag, Berlin.

Mead, J.L., Xie, H., Wang, S., Huang, H., 2018. Enhanced adhesion of ZnO nanowires during *in situ* scanning electron microscope peeling. Nanoscale 10, 3410–3420.

Nadler, B., Tang, T., 2008. Decohesion of a rigid punch from non-linear membrane undergoing finite axisymmetric deformation. International Journal of Non-Linear Mechanics 43, 716–721.

Nicholson, D.W., 1977. Peel mechanics with large bending. International Journal of Fracture 13, 279–287.

Nicolau, A.M., Huddleston, J.V., 1982. The compressible elastica on an elastic foundation. Journal of Applied Mechanics 49, 577–583.

Panayotounakos, D.E., 1989. Non-linear and buckling analysis of bars lying on elastic foundation. International Journal of Non-Linear Mechanics 24, 295–307.

Peng, Z.L., Yin, H., Yao, Y., Chen, S., 2019. Effect of thin-film length on the peeling behavior of film-substrate interfaces. Physical Review E 100, 032804.

Pesika, N.S., Tian, Y., Zhao, B., Rosenberg, K., Zeng, H., McGuiggan, P., Autumn, K., Israelachvili, J.N., 2007. Peel-zone model of tape peeling based on the gecko adhesive system. Journal of Adhesion 83, 383–401.

Plaut, R.H., 2010. Two-dimensional analysis of peeling adhesive tape from human skin. Journal of Adhesion 86, 1086–1110.

Plaut, R.H., Virgin, L.N., 2010. Vibrations and large postbuckling deflections of optimal pinned columns with elastic foundations. Structural and Multidisciplinary Optimization 40, 157–164.

Plaut, R.H., Virgin, L.N., 2014. Deformation and vibration of upright loops on a foundation and of hanging loops. International Journal of Solids and Structures 51, 3067–3075.

Plaut, R.H., Williams, N.L., Dillard, D.A., 2001. Elastic analysis of the loop tack test for pressure sensitive adhesives. Journal of Adhesion 76, 37–53.

Sasaki, N., Toyoda, A., Itamura, N., Miura, K., 2008. Simulation of nanoscale peeling and adhesion of single-walled carbon nanotube on graphite surface. e-Journal of Surface Science and Nanotechnology 6, 72–78.

Sasaki, N., Okamoto, H., Masuda, S., Miura, K., Itamura, N., 2010. Simulated nanoscale peeling process of monolayer graphene sheet: Effect of edge structure and lifting position. Journal of Nanomaterials 2010, 742127.

Seely, F., Smith, J., 1952. Advanced Mechanics of Materials, second ed. Wiley, New York.

Sekiguchi, Y., Hemthavy, P., Saito, S., Takahashi, K., 2012. Adhesion between side surface of an elastic beam and flat surface of a rigid body. Journal of Adhesion Science and Technology 26, 2615–2626.

Sekiguchi, Y., Hemthavy, P., Saito, S., Takahashi, K., 2014. Experiments of the adhesion behavior between an elastic beam and a substrate. International Journal of Adhesion and Adhesives 49, 1–6.

Skopic, B.H., Schniepp, H.C., 2020. Peeling in biological and bioinspired adhesive systems. JOM Journal of the Minerals Metals and Materials Society 72, 1509–1522.

Spies, G.J., 1953. The peeling test on redux-bonded joints: A theoretical analysis of the test devised by Aero Research Limited. Aircraft Eng. Aerospace Technol. 25, 64–70.

Strus, M.C., Zalamea, L., Raman, A., Pipes, R.B., Nguyen, C.V., Stach, E.A., 2008. Peeling force spectroscopy: Exposing the adhesive nanomechanics of one-dimensional nanostructures. Nano Letters 8, 544–550.

Strus, M.C., Cano, C.I., Pipes, R.B., Nguyen, C.V., Raman, A., 2009. Interfacial energy between carbon nanotubes and polymers measured from nanoscale peel tests in the atomic force microscope. Composites Science and Technology 69, 1580–1586.

Tysoe, W.T., Spencer, N.D., 2015. Gecko's feet and sticky tape. Tribology & Lubrication Technology 71, 108–110.

Vaz, M.A., Nascimento, M.S., Solano, R.F., 2007. Initial postbuckling of elastic rods subjected to thermal loads and resting on an elastic foundation. Journal of Thermal Stresses 30, 381–393.

Wan, X., He, Y., Chen, Y., Yang, C., 2021. Cohesive behaviors of hydrogel under large-scale bridging. Journal of Applied Mechanics 88, 111011.

Wang, S.J., Li, X., 2010. The coupling effect of punch shape and residual stress on measuring work of membrane by pull-off test. Thin Solid Films 518, 6036–6039.

Wang, W., Liu, Y., Xie, Z., 2021. Gecko-like dry adhesive surfaces and their applications: A review. Journal of Bionic Engineering 18, 1011–1044.

Williams, J.A., 2015. Adhesional instabilities and gecko locomotion. J. Physics D 48, 015401.

Wu, X., Wang, X., Mei, T., Sun, S., 2015. Mechanical analyses on the digital behaviour of the Tokay gecko (*Gekko gecko*) based on a multi-level directional adhesion model. Proceedings of the Royal Society A 471, 20150085.

Yin, H.B., Liang, L.H., Wei, Y.G., Peng, Z.L., Chen, S.H., 2020. Determination of the interface properties in an elastic film/substrate system. International Journal of Solids and Structures 191–192, 473–485.